Acta Mech
https://doi.org/10.1007/s00707-017-2010-5

ORIGINAL PAPER

Cunbao Li · Viet T. Chau · Heping Xie · Zdeněk P. Bažant

Recent advances in mechanics of fracking and new results on 2D simulation of crack branching in anisotropic gas or oil shale

This paper is dedicated to the memory of Franz Ziegler

Received: 19 April 2017 / Revised: 7 June 2017

Abstract This article presents a comprehensive overview of several recent theoretical results at Northwestern University and demonstrates them by new numerical simulations of branching of hydraulic fractures. To model the inelastic behavior and fracturing of shale as an inherently anisotropic material, the recently developed spherocylindrical microplane model is described. Regarding the spread and branching of hydraulic cracks during the fracking process, it is emphasized that two kinds of water flow must be simulated: (1) the Poiseuille flow through the hydraulic fractures and natural cracks and (2) the Darcy diffusion flow of leak-off water through the pores of intact shale. The body forces due to gradient of Darcy flow pressure must be taken into account. The crack opening width is computed by means of the crack band model, in which each finite element is imagined to contain at the outset a potential cohesive crack, one in each of three spatial orientations, with the fracking water flowing through if the crack gets opened. The use of this model to suppress problems of mesh sensitivity due to localization of distributed fracturing is explained. Computer simulations of the growth of branched hydraulic system are preformed in two dimensions (2D) only. The results illustrate the effects of anisotropy and natural cracks on the evolution of 2D fracture patterns during the fracking process. These effects are not large, but much stronger effects are expected in future three-dimensional simulations.

1 Introduction

Although hydraulic fracturing [1] (aka fracking, or frac process) has met with enormous success, its fracture mechanics is still poorly understood and major gaps of knowledge remain [2,3]. This may explain why only 5–15% of the gas contained in the shale strata is currently recovered. To increase this percentage requires

C. Li · V. T. Chau
Northwestern University, Evanston, IL, USA
E-mail: VietChau2017@u.northwestern.edu

C. Li · H. Xie
Key Laboratory of Energy Engineering Safety and Disaster Mechanics Ministry of Education, Sichuan University, Chengdu, China
E-mail: xiehp@scu.edu.cn

C. Li · H. Xie
College of Architecture and Environment, Sichuan University, Chengdu, China
E-mail: sculcb@gmail.com

Z. P. Bažant (✉)
McCormick Institute Professor and W.P. Murphy Professor of Civil and Mechanical Engineering and Materials Science, Northwestern University, 2145 Sheridan Road, CEE/A135, Evanston, IL 60208, USA
E-mail: z-bazant@northwestern.edu

Published online: 17 January 2018

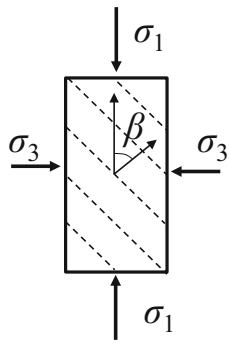

Fig. 1 Definition of the bedding layer (dash line) orientation

tackling several basic rock mechanics problems. This includes, though is not limited to, a constitutive model for fracture, progressive damage and frictional slip in the presence of material anisotropy.

Extensive experimental studies of the mechanical properties of shale exist now in the literature. They include the Brazilian split-cylinder tests [4], uniaxial and triaxial compression test [5,6], direct shear tests [7] and uniaxial and triaxial creep tests [8,9]. These test results demonstrate that the stiffness, strength and failure mode of shale depend strongly not only on the confinement but also on the loading direction with respect to the bedding layers (Fig. 1), which are the planes of rotational symmetry (or isotropy). The failure criteria for anisotropic geomaterials have also been studied extensively. Three kinds of these criteria may be distinguished: the mathematical continuum models [10–12], empirical continuum models [13] and discontinuous weakness plane models [14,15]. But all of them have some shortcomings; for example, the mathematical continuum models can describe rock failure in only one kind of failure mechanism [16].

A general constitutive model for finite element programs must do more than reproduce criteria for failure. It must also characterize the complete stress–strain relation for progressive failure, including the postpeak softening, and take into account the anisotropy of shale. Some advanced tensorial formulations [17–19] use irreversible thermodynamics and internal variables, which allows clarity in satisfying the thermodynamic restrictions. However, the use of stress and strain tensors, their invariants and internal variables, makes it difficult to capture the orientation of damage due to cracking and frictional slip. This is a serious limitation. For example, the dependence of the second invariant of the stress deviator, J_2, on the first stress invariant, I_1, is generally considered to characterize internal friction. However, in reality, the frictional slips occur only along planes of certain specific orientations. The same applies to the microcracks.

Many studies [20–27, e.g.] contributed to the present understanding of shale fracking. One perplexing feature was that the standard fracture mechanics models predict no branching of hydraulic cracks, typically ca. 10 m apart, while branched cracks of close spacing of the order of 0.1 m are required to explain the observed gas production rate [2]. It was thus thought that the preexisting natural cracks formed during circa one million years somehow increase the shale permeability on the large scale by four orders of magnitude. However, the recent formulation of a three-phase medium, in which the hydraulic pressures are supplemented by body forces due to pressure gradients of water diffusing into the scale, showed that crack branching can, and indeed must, occur [28]. At the same time it was shown that, over the geologic time span, any cracks caused by past tectonic upheavals must have been closed (at the typical depths of several kilometers) by primary and secondary creep of shale or must have gotten filled by calcite deposits [29]. Thus, it is nearly certain that the preexisting cracks or joints cannot significantly contribute to observed gas production.

The previous simulations of hydraulic crack branching [28] have been conducted with simplified constitutive models for shale because a realistic model for strength and inelastic deformations including the postpeak softening damage did not yet exist. Such a model has been developed in a preceding study [30] using the microplane modeling concept. The model is fully explicit, which is particularly advantageous for the microplane model. The basic idea is to capture the anisotropy, particularly the transverse isotropy, by combining the classical spherical microplane system with a cylindrical microplane system whole axis is normal to the plane of orthotropy (i.e., to the bedding planes). Material anisotropy or orthotropy presents particular difficulties for the modeling of inelastic behavior [31], and the microplane approach, based on vectors rather than tensors, is the most effective way to overcome them.

The objective of this paper is twofold: (1) to provide a unified review of the recent advances in the mechanics of hydraulic fracturing and on the constitutive modeling of inelastic behavior of gas or oil shale, taking into

account its innate anisotropy due to bedding layers in shale and (2) to present new computational results documenting the difference between the presence or absence of closed natural cracks with zero strength, and the effects of anisotropy, particularly the orientation of the bedding layer orientation. Due to size limitation, the review part is focused on the advances made at the authors' home institution and particularly on the new anisotropic spherocylindrical microplane model.

2 Overview of spherocylindrical microplane model

2.1 General classical framework

Although the microplane model was originally developed for softening damage in isotropic materials, it is well suited to capture material anisotropy, elastic as well as inelastic. There are many possibilities. Introducing microplane weights depending on the polar angle θ gave realistic results for the foam core of a sandwich shell, for which the ratio of in-plane to out-of-plane moduli, E_{xx}/E_{yy}, is about 2 [32]. For textile fiber composite laminates, this approach turned out to be inadequate, and three different orthotropic versions were devised: (1) the spectral stiffness microplane model [33], which can reproduce the most general elastic orthotropy but is cumbersome in data fitting and not well suited for deriving material properties from those of constituents, (2) a model with the microplanes arranged so as to capture braided fiber undulation [34] and (3) microplane triad model, which captures better the in-plane lateral interactions of the yarns [35]. But none of these approaches work for shale, which has a layered structure usually subjected (in contrast to the laminates) to large transverse compression, for which the material strength and stiffness depend on θ nonmonotonically.

The *spherocylindrical* microplane model combines spherical and cylindrical microplane systems, called *phases*; see Fig. 2, in which the classical three-dimensional (3D) spherical microplane phase is considered to be coupled in parallel with a two-dimensional (2D) cylindrical microplane phase subjected to the same kinematic constrain, i.e., to the same strain tensor ϵ_{ij} ($i, j = 1, 2, 3$ are Cartesian subscripts). The stress tensors carried by the spherical and cylindrical microplane phases are assumed to be $\alpha\sigma_{ij}$ and $(1-\alpha)\sigma_{ij}$, respectively, where σ is the continuum (or macroscale) stress tensor and α is the volumetric fraction of the spherical phase.

The spatial orientations of the microplane normals of the spherical phase follow the optimal Gaussian numerical integration formula for a spherical surface [36] (Fig. 2a). These orientations or the numerical integration points cannot be distributed over the spherical surface uniformly and thus require nonuniform weights, w_μ [36]. By contrast, for cylindrical phase, one may distribute the numerical integration points along a unit circle uniformly (Fig. 2a), with equal weights $1/N_c$ regardless of the number, N_c, of points (or cylindrical microplanes). Because the microplanes on opposite sides of the circle represent the same stress–strain state, it suffices to integrate (or sum) over only a half-circle and then multiply the result by 2.

According to the kinematic constraint [37], the components of the strain vectors $\vec{\epsilon}_N^s$ (Fig. 2b) and $\vec{\epsilon}_N^c$ (Fig. 2c) on the spherical and cylindrical microplanes are $\epsilon_{Ni}^s = \epsilon_{ij} n_j^s$ and $\epsilon_{Ni}^c = \epsilon_{ij} n_j^c$, where n_j^s and n_j^c are the components of the unit normal vectors $\boldsymbol{n}^s$ and $\boldsymbol{n}^c$ defining the microplane position. The components of the strain vectors on the spherical and cylindrical microplanes are calculated as follows:

$$\epsilon_N^s = \epsilon_{ij} N_{ij}^s, \quad \epsilon_L^s = \epsilon_{ij} L_{ij}^s, \quad \epsilon_M^s = \epsilon_{ij} M_{ij}^s, \tag{1}$$

$$\epsilon_N^c = \epsilon_{ij} N_{ij}^c, \quad \epsilon_L^c = \epsilon_{ij} L_{ij}^c, \quad \epsilon_M^s = \epsilon_{ij} M_{ij}^c, \tag{2}$$

where repetition of subscripts implies summation over $i = 1, 2, 3$, and

$$N_{ij}^s = n_i^s n_j^s, \quad L_{ij}^s = \left(l_i^s n_j^s + l_j^s n_i^s\right)/2, \quad M_{ij}^s = \left(m_i^s n_j^s + m_j^s n_i^s\right)/2, \tag{3}$$

$$N_{ij}^c = n_i^c n_j^c, \quad L_{ij}^c = \left(l_i^c n_j^c + l_j^c n_i^c\right)/2, \quad M_{ij}^c = \left(m_i^c n_j^c + m_j^c n_i^c\right)/2. \tag{4}$$

Here l_i^s, m_i^s, l_i^c and m_i^c ($i = 1, 2, 3$) are the components of the unit vector $\boldsymbol{l}^s$, $\boldsymbol{m}^s$, $\boldsymbol{l}^c$ and $\boldsymbol{m}^c$, respectively.

Numerical simulations prove that realistic modeling of the inelastic behavior in compression necessitates the volumetric–deviatoric split, in which the deviatoric strain on the spherical microplane is defined as

$$\epsilon_D^s = \epsilon_N^s - \epsilon_V, \quad \epsilon_V = \epsilon_{kk}/3, \tag{5}$$

where ϵ_V is volumetric (or mean) strain, which is the same for all the spherical microplanes.

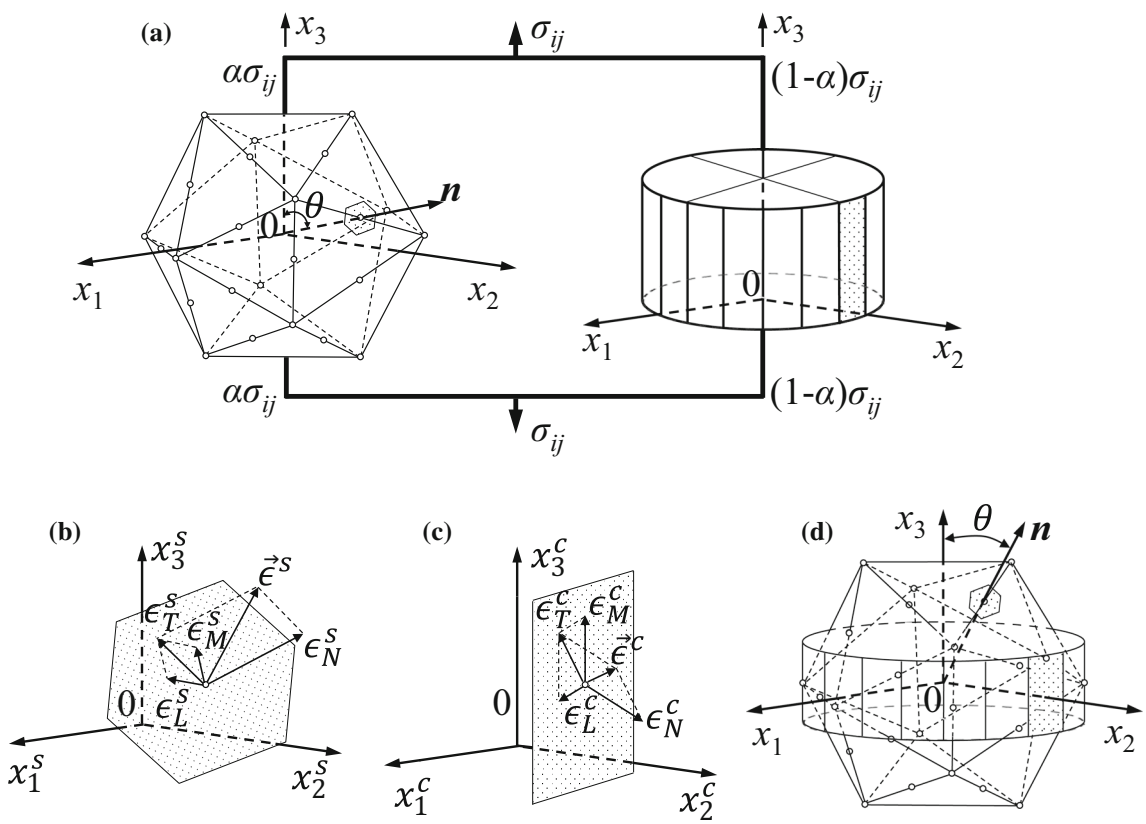

Fig. 2 **a** Spherocylindrical microplane configuration; left: spherical microplane configuration; right: cylindrical microplane configuration; **b** microplane strain components on the spherical microplane; **c** microplane strain components on the cylindrical microplane; and **d** another diagram of the paralleled spherocylindrical microplane configuration

The relationship between the stress tensor on the macroscopic (continuum) scale with the stress vectors on the microplanes may best be determined from the principle of virtual work, i.e., the sum of the virtual works of all the microplane stress vectors must be equal to the virtual work of macroscopic stress tensor:

$$\sigma_{ij} = \alpha \frac{3}{2\pi} \int_{\Omega} \left(\sigma_N^{\mathrm{s}} N_{ij}^{\mathrm{s}} + \sigma_L^{\mathrm{s}} L_{ij}^{\mathrm{s}} + \sigma_M^{\mathrm{s}} M_{ij}^{\mathrm{s}} \right) \mathrm{d}\Omega + (1-\alpha) \frac{1}{\pi} \int_{S} \left(\sigma_N^{\mathrm{c}} N_{ij}^{\mathrm{c}} + \sigma_L^{\mathrm{c}} L_{ij}^{\mathrm{c}} + \sigma_M^{\mathrm{c}} M_{ij}^{\mathrm{c}} \right) \mathrm{d}S \tag{6}$$

$$\approx 6\alpha \sum_{\mu=1}^{N_{\mathrm{m}}^{\mathrm{s}}} w_{\mu}^{\mathrm{s}} \left(\sigma_N^{\mathrm{s}} N_{ij}^{\mathrm{s}} + \sigma_L^{\mathrm{s}} L_{ij}^{\mathrm{s}} + \sigma_M^{\mathrm{s}} M_{ij}^{\mathrm{s}} \right)_{(\mu)} + (1-\alpha) \frac{1}{\pi N_{\mathrm{m}}^{\mathrm{c}}} \sum_{\mu=1}^{N_{\mathrm{m}}^{\mathrm{c}}} \left(\sigma_N^{\mathrm{c}} N_{ij}^{\mathrm{c}} + \sigma_L^{\mathrm{c}} L_{ij}^{\mathrm{c}} + \sigma_M^{\mathrm{c}} M_{ij}^{\mathrm{c}} \right)_{(\mu)} . \tag{7}$$

Here α is the volumetric fraction of the spherical phase; Ω is the surface of a unit hemisphere; S is the lateral surface of a unit cylinder; $N_{\mathrm{m}}^{\mathrm{s}}$ and $N_{\mathrm{m}}^{\mathrm{s}}$ are the total numbers of microplanes per hemisphere and per half-circle, respectively; w_{μ}^{s} are the weights in the optimal Gaussian numerical formula for spherical surface; and the subscript (μ) labels the contribution of the μth microplane to the total macroscopic stress tensor. For the cylinder, equal weights with a uniform subdivision are optimal.

2.2 Essentials of microplane modeling of elastic and inelastic behavior of shale

When the elastic behavior is characterized on the microplane level, two simplifications are possible:

1. Prior to reaching the strength limit, the elastic moduli on the microplanes can be considered constant if the loading on the microplane is monotonic. This approximation works not only for the normal and

shear components of the strain vector, but also for the volumetric and deviatoric components. The prepeak nonlinearity and prepeak path dependence are generated automatically, thanks to the fact that, during loading, different microplanes reach their strength limits at different times. Physically, this corresponds to gradual formation of microcracks and microslips during the loading progress.

2. The stress–strain relations for different strain components on the microplanes on the microplanes can be considered decoupled because, as experience indicates, they are approximately captured by interactions between microplanes of different orientations.

Consequently,

$$\sigma_V = E_V \epsilon_V, \quad \sigma_N^{\mathrm{s}} = E_N^{\mathrm{c}} \epsilon_N^{\mathrm{s}}, \quad \sigma_D^{\mathrm{s}} = E_D^{\mathrm{s}} \epsilon_D^{\mathrm{s}}, \quad \sigma_M^{\mathrm{s}} = E_M^{\mathrm{s}} \epsilon_M^{\mathrm{s}}, \quad \sigma_L^{\mathrm{s}} = E_L^{\mathrm{s}} \epsilon_L^{\mathrm{s}}, \tag{8}$$

$$\sigma_N^{\mathrm{c}} = E_N^{\mathrm{c}} \epsilon_N^{\mathrm{c}}, \quad \sigma_L^{\mathrm{c}} = E_L^{\mathrm{c}} \epsilon_L^{\mathrm{c}}, \quad \sigma_M^{\mathrm{c}} = E_M^{\mathrm{c}} \epsilon_M^{\mathrm{c}}, \tag{9}$$

where E_V, E_N^{s}, E_D^{s}, E_L^{s}, E_M^{s}, E_N^{c}, E_L^{c}, E_M^{c} are the elastic parameters on the microplane, which are considered as independent of microplane orientation.

Substituting Eqs. (8) and (9) into Eq. (6), one can get the macroscopic stiffness $\bar{C}_{ijkl}$ as:

$$\begin{aligned}\bar{C}_{ijkl} = \alpha \frac{3}{2\pi} \int_\Omega \left(E_D^{\mathrm{s}} N_{ij}^{\mathrm{s}} N_{kl}^{\mathrm{s}} + \frac{1}{3} \left(E_V - E_D^{\mathrm{s}} \right) N_{ij}^{\mathrm{s}} \delta_{kl} + E_L^{\mathrm{s}} L_{ij}^{\mathrm{s}} L_{kl}^{\mathrm{s}} + E_M^{\mathrm{s}} M_{ij}^{\mathrm{s}} M_{kl}^{\mathrm{s}} \right) \mathrm{d}\Omega \\ + (1-\alpha) \frac{1}{\pi} \int_S \left(E_N^{\mathrm{c}} N_{ij}^{\mathrm{c}} N_{kl}^{\mathrm{c}} + E_L^{\mathrm{c}} L_{ij}^{\mathrm{c}} L_{kl}^{\mathrm{c}} + E_M^{\mathrm{c}} M_{ij}^{\mathrm{c}} M_{kl}^{\mathrm{c}} \right) \mathrm{d}S.\end{aligned} \tag{10}$$

Comparisons of components with the same subscript combinations on the left and right sides of Eq. (10) and the kinematic constraint with volumetric–deviatoric split yield the following expressions for the microplane elastic constants:

$$E_V = (C_{33} + 2C_{13})/\alpha, \tag{11}$$

$$E_L^{\mathrm{s}} = E_M^{\mathrm{s}} = E_T^{\mathrm{s}} = (C_{33} - C_{13})/\alpha, \tag{12}$$

$$E_D^{\mathrm{s}} = (C_{33} - C_{13})/\alpha, \tag{13}$$

$$E_N^{\mathrm{c}} = 2(C_{11} - C_{33} + C_{12} - C_{13})/(1-\alpha), \tag{14}$$

$$E_L^{\mathrm{c}} = 2(C_{11} - C_{33} - 3C_{12} + 3C_{13})/(1-\alpha), \tag{15}$$

$$E_M^{\mathrm{c}} = 4(2C_{44} - C_{33} + C_{13})/(1-\alpha), \tag{16}$$

where C_{11}, C_{12}, C_{13}, C_{33} and C_{44} are the five independent components of the transversely isotropic elastic stiffness matrix C_{IJ}, which represents the symmetric fourth-order tensor $\bar{C}_{ijkl}$ in the Voigt notation.

Let $\Delta\epsilon_V$, $\Delta\epsilon_D^{\mathrm{s}}$, $\Delta\epsilon_L^{\mathrm{s}}$, $\Delta\epsilon_M^{\mathrm{s}}$, $\Delta\epsilon_N^{\mathrm{c}}$, $\Delta\epsilon_L^{\mathrm{s}}$ and $\Delta\epsilon_M^{\mathrm{c}}$ be the microplane strain increments in a finite loading step. The elastic stresses on the microplanes at the end of the loading step are obtained as

$$\sigma_V = \sigma_V^{(0)} + E_V \Delta\epsilon_V, \tag{17}$$

$$\sigma_D^{\mathrm{s}} = \sigma_D^{s(0)} + E_D^{\mathrm{s}} \Delta\epsilon_D^{\mathrm{s}}, \tag{18}$$

$$\sigma_L^{\mathrm{s}} = \sigma_L^{s(0)} + E_L^{\mathrm{s}} \Delta\epsilon_L^{\mathrm{s}}, \tag{19}$$

$$\sigma_M^{\mathrm{s}} = \sigma_M^{s(0)} + E_L^{\mathrm{s}} \Delta\epsilon_M^{\mathrm{s}}, \tag{20}$$

$$\sigma_N^{\mathrm{c}} = \sigma_N^{c(0)} + E_N^{\mathrm{c}} \Delta\epsilon_N^{\mathrm{c}}, \tag{21}$$

$$\sigma_L^{\mathrm{c}} = \sigma_L^{c(0)} + E_L^{\mathrm{c}} \Delta\epsilon_L^{\mathrm{c}}, \tag{22}$$

$$\sigma_M^{\mathrm{c}} = \sigma_M^{c(0)} + E_M^{\mathrm{c}} \Delta\epsilon_M^{\mathrm{c}}, \tag{23}$$

where a superscript (0) labels the initial stresses, as calculated in the previous loading step, while the elastic stresses at the end of the current loading step are labeled by no subscript.

The inelastic behavior is effectively described by the so-called stress–strain boundaries [38], which represent strain-dependent strength limits on the microplanes. Within the boundaries, the response is elastic. If the boundary is exceeded in a finite time step or loading step, the microplane stress drops at constant strain to the boundary while keeping the strain constant. (This is actually a special case of the radial return algorithm.) Despite the abrupt slope changes when a microplane stress reaches the boundary, the macroscopic response

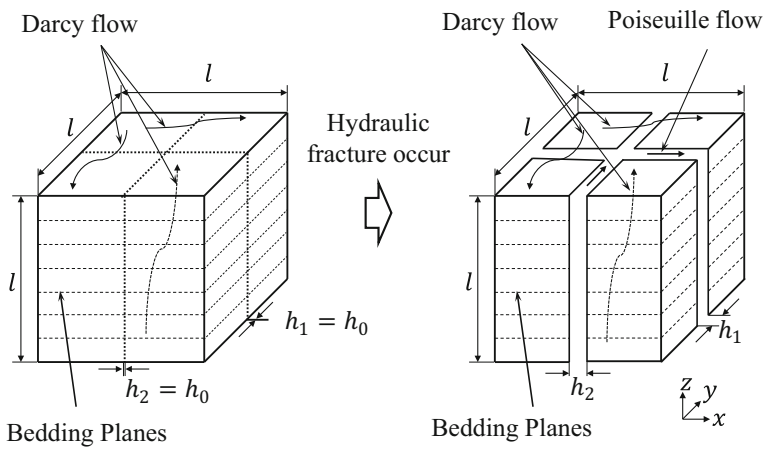

Fig. 3 Typical finite element of shale with potential vertical cracks (left) or with cracks already formed (right)

is quite smooth because different microplanes reach the boundary (or enter the unloading regime) at different times. This approach has the advantage several independent boundaries for different stress components on the microplane can be defined as functions of the corresponding strain components.

Accordingly, the strength limit for each microplane stress component of the spherical phase can be defined as

$$\sigma_N^{sb+} = f(\theta) F_N^{\mathrm{s}} \left(\epsilon_N^{\mathrm{s}}, \epsilon_V\right), \quad \sigma_D^{sb+} = f(\theta) F_D^{\mathrm{s}+} \left(\epsilon_D^{\mathrm{s}}\right), \quad \sigma_D^{sb-} = h(\theta) F_D^{s-} \left(-\epsilon_D^{\mathrm{s}}\right), \quad \sigma_T^{sb} = g(\theta) F_T^{\mathrm{s}} \left(\sigma_N^{\mathrm{s}}\right), \tag{24}$$

where

$$\sigma_T^{\mathrm{s}} = \sqrt{\left(\sigma_L^{\mathrm{s}}\right)^2 + \left(\sigma_M^{\mathrm{s}}\right)^2}. \tag{25}$$

Similar to the spherical phase, the strength limit for each microplane stress component of the cylindrical phase can be defined as

$$\sigma_N^{cb+} = F_N^{\mathrm{c}+} \left(\epsilon_N^{\mathrm{c}}, \epsilon_V\right), \quad \sigma_D^{cb-} = F_D^{\mathrm{c}-} \left(-\epsilon_N^{\mathrm{c}}, \epsilon_V\right), \quad \sigma_T^{cb} = F_T^{\mathrm{c}} \left(\sigma_N^{\mathrm{c}}\right), \tag{26}$$

where

$$\sigma_T^{\mathrm{c}} = \sqrt{\left(\sigma_L^{\mathrm{c}}\right)^2 + \left(\sigma_M^{\mathrm{c}}\right)^2}. \tag{27}$$

A detailed discussion of the stress–strain boundaries and numerical algorithm is given in [30].

3 Modeling of liquid flow through cracks and pores

The fluid pressure in fracking is generally less than the overburden pressure. Consequently, all the cracks and joints are assumed to be vertical, and no horizontal cracks are formed. One system of parallel distributed cracks is expected to be normal to the minimum principal tectonic stress σ_h. The second system of parallel distributed cracks is expected to be nearly orthogonal to the first (and thus normal to the maximum principal tectonic stress σ_H). The reason is that if the cracks in one system of parallel cracks are open and thus free of shear stresses, then the open cracks in a second intersecting system can also be free of shear stresses only if the systems are orthogonal, as required for local equilibrium. The size of the finite elements of shale (Fig. 3) is considered to be equal to the minimum possible spacing l of parallel hydraulic cracks.

As argued in [28], two kinds of fluid transport must be considered: One is the Poiseuille flow along the hydraulic fractures or hydraulically opened natural fractures, and the other one is the diffusion flow through the preexisting pores, as shown in Fig. 3. Since the pores size in gas shale ranges from less than 1 nm to hundreds nm, various types of diffusion including Darcy flow, Knudsen flow and surface diffusion, [39,40],

may occur. However, since precise information on the type of diffusion is unavailable, we consider, for the sake of simplicity, the Darcy diffusion with constant diffusivity.

The flow along the hydraulically created cracks and hydraulically opened natural cracks can be assumed to follow the Reynolds equations of classical lubrication theory, which are based on the Poiseuille law for viscous flow. For the components q_i $(i = x, y, z)$ of the flux vectors in the vertical (x, z) and (y, z) crack planes, the governing equations are:

$$q_x = -\frac{h_1^2}{12\mu}\frac{\partial p}{\partial x}, \tag{28}$$

$$q_y = -\frac{h_2^2}{12\mu}\frac{\partial p}{\partial y}, \tag{29}$$

$$q_z = -\frac{h_1^2}{12\mu}\frac{\partial p}{\partial z} - \frac{h_2^2}{12\mu}\frac{\partial p}{\partial z}. \tag{30}$$

Here p is the fluid pressure in the cracks; h_1 and h_2 are the crack widths in the (x, z) and (y, z) planes; μ is the effective viscosity of the fracking fluid (including the effect of proppants). Equation (30) describes vertical flux components in both cracks.

The flow of fracking fluid through the pores is described by the Darcy law:

$$\hat{q}_x = \frac{\kappa_x}{\hat{\mu}}\frac{\partial \hat{p}}{\partial x}, \tag{31}$$

$$\hat{q}_y = \frac{\kappa_y}{\hat{\mu}}\frac{\partial \hat{p}}{\partial y}, \tag{32}$$

$$\hat{q}_z = \frac{\kappa_z}{\hat{\mu}}\frac{\partial \hat{p}}{\partial z}. \tag{33}$$

Here $\hat{q}_i$ $(i = 1, 2, 3$ or $x, y, z)$ are the components of volumetric flow rate through the pores in different directions; $\hat{\mu}$ is the viscosity (no proppant here); κ_i is the permeability of shale along the three orthogonal directions. The permeabilities in directions x, y of the isotropic plane (x, y) (i.e., along the bedding layers) can be considered the same, while the one in the transverse (vertical) direction is typically an order of magnitude smaller, i.e., $\kappa_x = \kappa_y \gg \kappa_z$, and thus κ_z is neglected in the computations.

The total flux Q_i is obtained by summing the fluxes through the cracks and pores:

$$Q_1 = h_1\left(-\frac{h_1^2}{12\mu}\frac{\partial p}{\partial x}\right) + (l - h_1)\left(\frac{\kappa_x}{\hat{\mu}}\frac{\partial \hat{p}}{\partial x}\right), \tag{34}$$

$$Q_2 = h_2\left(-\frac{h_2^2}{12\mu}\frac{\partial p}{\partial y}\right) + (l - h_2)\left(\frac{\kappa_y}{\hat{\mu}}\frac{\partial \hat{p}}{\partial y}\right), \tag{35}$$

$$Q_3 = -h_1\frac{h_1^2}{12\mu}\frac{\partial p}{\partial z} - h_2\frac{h_2^2}{12\mu}\frac{\partial p}{\partial z}. \tag{36}$$

Here l is the finite element size, assumed to be equal to the spacing of parallel cracks, about 0.1 m [2]. With this element size, the local stress and flow fields at a sharp crack tip cannot be captured, but the effective global energy dissipation at the front of a zone of many growing hydraulic cracks can. For the sake of simplification, the fluid pressure in the cracks and in the pores is considered to be the same within one finite element, and then, the fluid mass conservation equation can be expressed as:

$$\begin{aligned}
&\frac{\partial}{\partial t}(\rho h_1) - \frac{\partial}{\partial x}\left(\rho h_1\frac{h_1^2}{12\mu}\frac{\partial p}{\partial x}\right) - \frac{\partial}{\partial z}\left(\rho h_1\frac{h_1^2}{12\mu}\frac{\partial p}{\partial z}\right) + \frac{\partial}{\partial t}(\rho h_2) - \frac{\partial}{\partial y}\left(\rho h_2\frac{h_2^2}{12\mu}\frac{\partial p}{\partial y}\right)\\
&\quad - \frac{\partial}{\partial z}\left(\rho h_2\frac{h_2^2}{12\mu}\frac{\partial p}{\partial z}\right) + \frac{\partial}{\partial t}[\rho\phi(l - h_1)] - \frac{\partial}{\partial x}\left[\rho(l - h_1)\frac{\kappa_x}{\mu}\frac{\partial p}{\partial x}\right] + \frac{\partial}{\partial t}[\rho\phi(l - h_2)]\\
&\quad - \frac{\partial}{\partial y}\left[\rho(l - h_2)\frac{\kappa_y}{\mu}\frac{\partial p}{\partial y}\right] + \frac{\partial}{\partial t}\left[\rho\phi\frac{(l - h_1)(l - h_2)}{l}\right] = 0.
\end{aligned} \tag{37}$$

Here, ϕ is the porosity of shale; ρ is the mass density of fluid, which has been considered as incompressible in most of previous studies of hydraulic fracturing simulation. But the mass density of fluid has influence on the pressure changes due to rock deformation changes, and these affect the flow rate. Further it matters for the flow and local stress field near the crack front. So the mass density of the fluid is considered to be dependent on the pressure p as:

$$\rho = \rho_0[1 + C_{\mathrm{f}}(p - p_0)]. \tag{38}$$

Here, C_{f} is the compressibility of fluid (which is an order-of-magnitude greater than that of shale); ρ_0 is the mass density at the references pressure p_0, which can be taken as the atmospheric pressure.

4 Crack band model versus RVE size

To capture the nonlocality of fracturing, the present computations use the crack band model [41–44]. This model is a simple and effective way to handle the propagation of cracks in quasibrittle materials characterized by a wide fracture process zone with progressive strain-softening damage at crack front. Without any special measures, the strain-softening leads to ill-posedness of the boundary value problem and spurious mesh sensitivity in finite element computations [44]. In nonlinear finite element analysis, the ill-posedness gets manifested by loss of convergence [43].

A simple remedy for the spurious mesh sensitivity caused by the strain softening is to adopt the crack band model. Compared to the cohesive crack model, one important advantage is that the tensorial state in the fracture process zone, especially the weakening effect of the compressive stresses parallel to the crack plane, can be taken into account. So can the mixed mode, with normal and shear stresses.

The basic idea of this model is that: (1) to the extent possible, the finite element size should be kept the same as the size of material test specimens for which the constitutive model has been calibrated (provided that the specimens were small enough to deform roughly homogeneously), and (2) if the finite element size must be increased, then the material parameters that control the smeared cracking strain must be adjusted in such a way that the energies dissipated by large and small elements per unit length and width of the crack band front would be identical; i.e.,

$$h_{\mathrm{c}}\gamma_{\mathrm{F}} = h^{\mathrm{e}}\gamma_{\mathrm{F}}^{\mathrm{e}} = G_{\mathrm{F}}. \tag{39}$$

Here h_{c} and γ_{F} are the material characteristic length and fracture energy density, both of which are material constants; h^{e} is the chosen size of finite element at fracture front, $\gamma_{\mathrm{F}}^{\mathrm{e}}$ is the density of fracture energy to be used for this element, and G_{F} is the fracture energy of the material.

5 Postpeak softening and the problem of finite element size versus RVE size

A noteworthy consequence of Eq. (39) is that the reference finite element can be much larger than the representative volume element (RVE) of the material, provided that this element has about the same size as the test specimens by which the constitutive model has been calibrated. Here an important new experimental result of Hull and Abousleiman [45] calls for an update of the constitutive model calibration. Since no tensile experimental data on postpeak softening in shale exist, the postpeak softening of the spherocylindrical microplane model to be described next is assumed to be similar to that of concrete. It is not surprising that this has not been perfect.

Hull et al.'s experimental results reveal the existence of a gradual postpeak softening in tensile bending fracture. Their tests used shale cantilevers with the cross-sectional depth of about 10 μm, loaded by an AFM (atomic force microscope). These tests imply that the RVE size of shale for tensile fracturing is far smaller than expected—probably of the order of 0.01 mm, for tension. But in compression, the RVE size could be far larger. Yet the postpeak softening and the implied RVE size have rarely been analyzed in compression. This, too, might have been caused by the RVE being much smaller than the specimen size, but it could also have been caused by insufficient stiffness of the test system. Fortunately, for fracking simulations, the RVE size in compression is not too important because, in hydraulic fracturing, the shale is never made to collapse in compression. This fact is confirmed by the present and previous computer simulations, which never lead to compression softening of the shale. Therefore, revising the postpeak compression characteristic of the spherocylindrical model to be discussed next is not very important (although the fact that some microplanes enter postpeak softening before

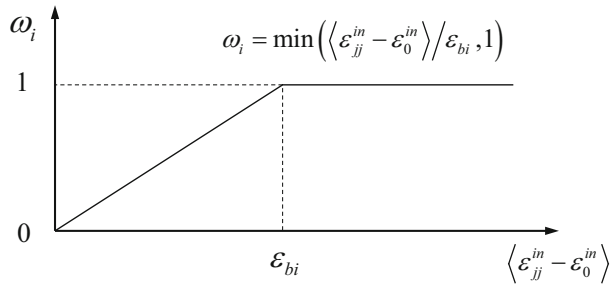

(a) Damage evolution of hydraulic fractures

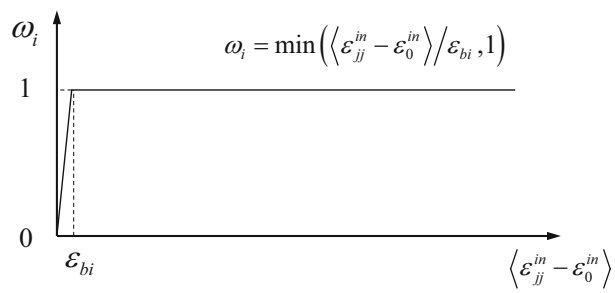

(b) Damage evolution of natural fractures

Fig. 4 Schematic diagram in damage evolution in hydraulic fractures and natural fractures ($i, j = 1, 2$ and $i \neq j$; Einstein's summation convention is not used here)

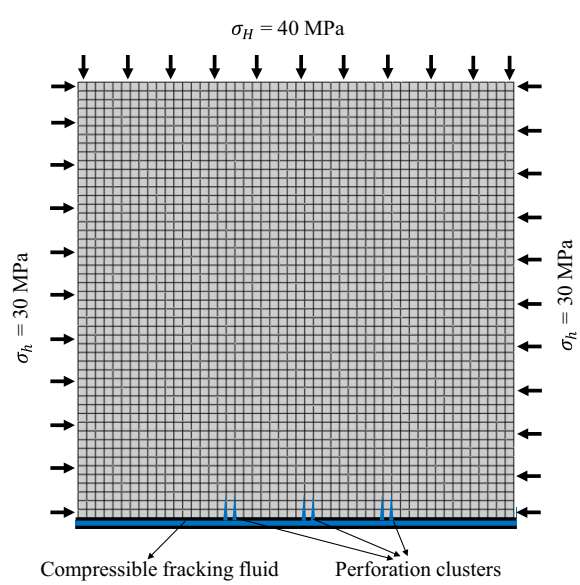

Fig. 5 Numerical model of hydraulic fracturing

the macro-level peak load is reached plays some role). As for tension, the postpeak tension characteristics of this model should, in principle, be revised (for the practical element size used), to capture the fracture energy in tension properly.

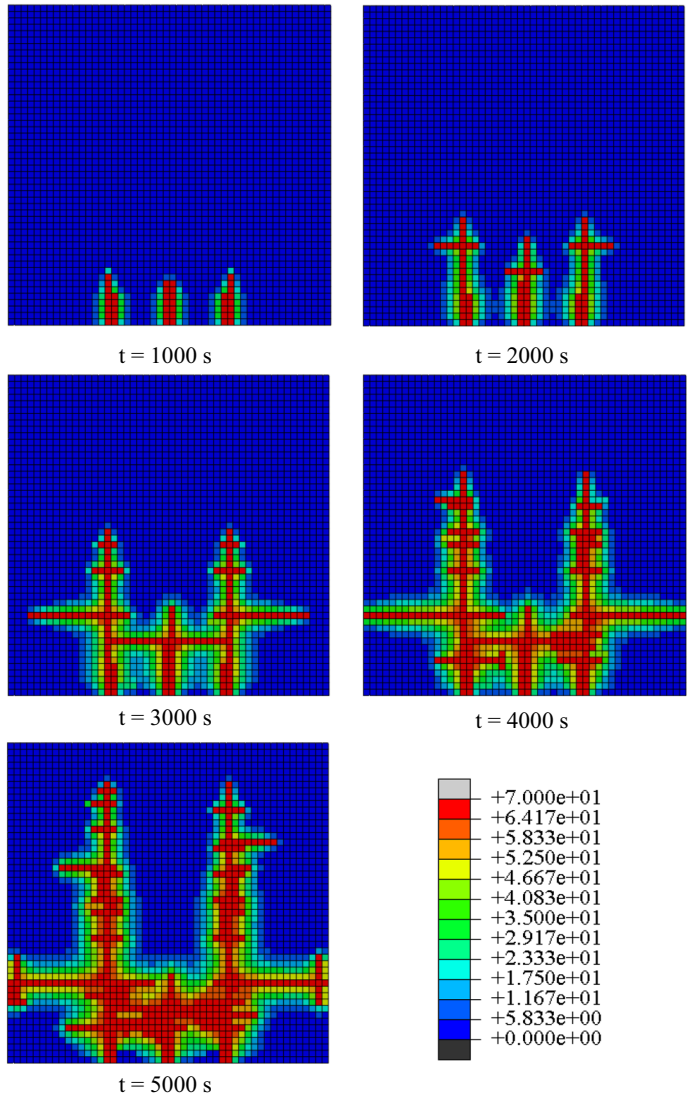

Fig. 6 The distribution of hydraulic pressure when the bedding layer orientation is 0° and without considering natural crack (the red indicates open cracks) (colour figure online)

6 Coupling between shale deformation, crack opening and flow equations

The crack width is computed based on the crack band model and smeared crack theory [41,44], in which each element is imagined to contain at the outset one (and only one) potential cohesive crack, with fracking fluid flowing through if the crack gets formed.

This approach can avoid the problems of strain localization and spurious mesh sensitivity in simulation. The hydraulic crack widths h_1 and h_2 (Fig. 3) are computed from the continuum inelastic strain:

$$h_1 = l\left\langle \epsilon_{22}^{\text{in}} - \epsilon_0^{\text{in}} \right\rangle, \quad h_2 = l\left\langle \epsilon_{11}^{\text{in}} - \epsilon_0^{\text{in}} \right\rangle, \tag{40}$$

$$\epsilon_{11}^{\text{in}} = \epsilon_{11} - \epsilon_{11}^{\text{e}}, \quad \epsilon_{22}^{\text{in}} = \epsilon_{22} - \epsilon_{22}^{\text{e}}. \tag{41}$$

Here $\epsilon_{11}^{\text{in}}$ and $\epsilon_{22}^{\text{in}}$ are the inelastic strains in the directions x and y, which are calculated from Eq. (41); ϵ_{11} and ϵ_{22} are the total strains computed by the spherocylindrical microplane model; ϵ_{11}^{e} and ϵ_{22}^{e} are the elastic strains based on anisotropic elastic mechanics; ϵ_0^{in} is the inelastic strain threshold, i.e., the threshold at which the crack begins to open.

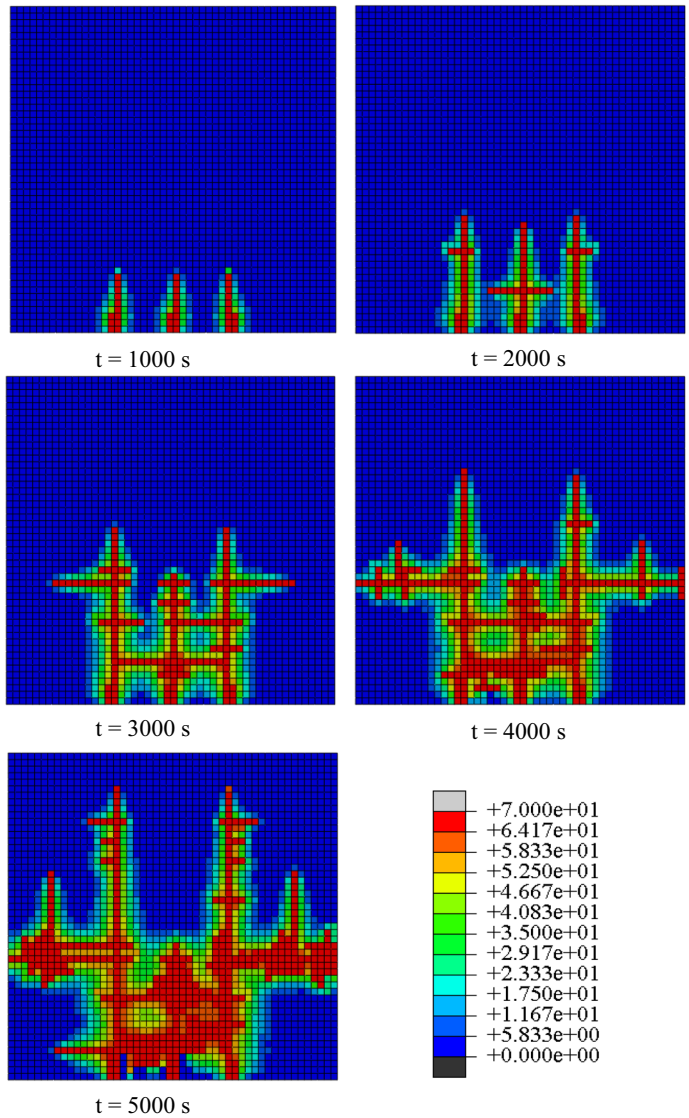

Fig. 7 The distribution of hydraulic pressure when the bedding layer orientation is 45° and without considering natural cracks

To characterize the damage induced by the distributed microcracks, two transverse isotropic damage factors are also defined according to the inelastic strain:

$$w_1 = \min\left(\left\langle \epsilon_{22}^{\text{in}} - \epsilon_0^{\text{in}} \right\rangle / \epsilon_{b1}, 1\right), \quad w_2 = \min\left(\left\langle \epsilon_{11}^{\text{in}} - \epsilon_0^{\text{in}} \right\rangle / \epsilon_{b2}, 1\right). \tag{42}$$

Here w_1 and w_2 are the two damage factors in the directions x and y; ϵ_{b1} and ϵ_{b2} are the breaking strain limits in two different directions. Based on Eq. (42), the natural cracks can be modeled by setting the strength and fracture energy in the finite element to be either zero or much lower than that of intact shale, as shown in Fig. 4.

The RVE of shale contains three phases: the solid shale, the cracks and the pores, which represents an amalgamation and generalization of both Biot's two-phase medium and Terzaghi's effective stress concept. For the configuration shown in Fig. 3, the effective stress of the RVE of shale can be expressed as

$$\begin{aligned}
s_{11} &= \sigma_{11} - w_1 p - (1 - w_1) r_{\text{b}} p, \\
s_{22} &= \sigma_{22} - w_2 p - (1 - w_2) r_{\text{b}} p, \\
s_{33} &= \sigma_{33} - r_{\text{b}} p, \\
s_{12} &= \sigma_{12},
\end{aligned}$$

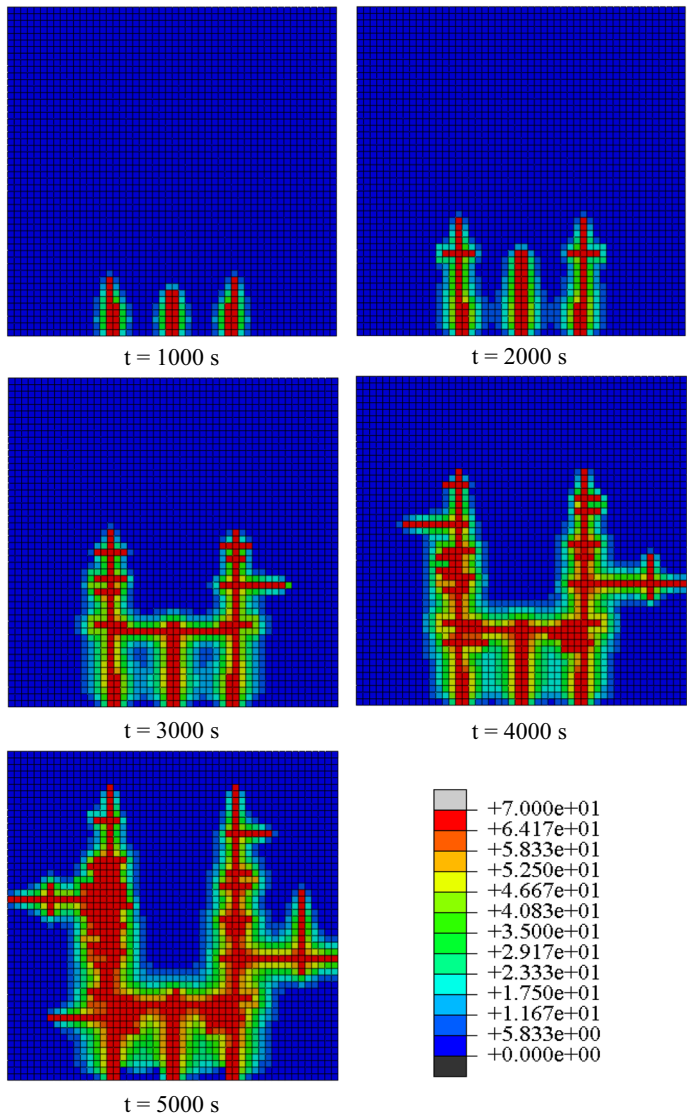

Fig. 8 The distribution of hydraulic pressure when the bedding layer orientation is 90° and without considering natural cracks

$$
\begin{aligned}
s_{13} &= \sigma_{13}, \\
s_{23} &= \sigma_{23}.
\end{aligned}
\tag{43}
$$

Here r_b is the Biot parameter. It is interesting to note that, if there are no cracks with damage, $w_1 = w_2 = 0$. Taking the one-dimensional case as a simple 1D prototype, Eq. (43) reduces to $s_{11} = \sigma_{11} - r_b p$. This is the well-known equilibrium relation for the total stress in Biot's two-phase medium. On the other hand, if the damage is complete, i.e., if $w_1 = w_2 = 1$ (crack-crossing bridges no longer exist), Eq. (43) reduces to $s_{11} = \sigma_{11} - p$, which is the well-known Terzaghi effective stress. Therefore, the present three-phase medium represents a continuous transition between these two classical fundamental concepts of soil mechanics.

7 Growth of branched hydraulic crack system showing effects of anisotropy and natural joints

The complete model just described has been used to clarify the importance of (1) the degree of anisotropy of shale and of (2) the tensile strength f_t and fracture energy G_f of the crack band model as well as the natural cracks for shale.

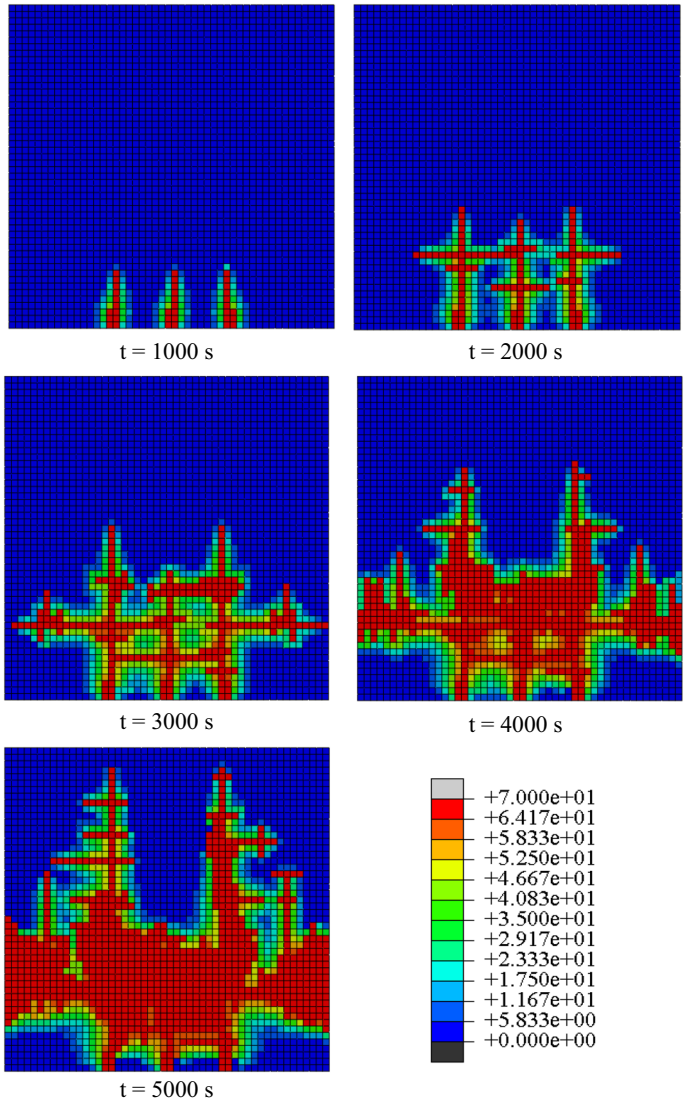

Fig. 9 The distribution of hydraulic pressure when the bedding layer orientation is 0° and with considering natural cracks

In the present coupled model, the nodal displacements of the shale and interelement fluxes of fluid are the basic unknown parameters. The deformation of shale is computed by the finite element method, and the flow of fluid through the opened cracks is computed by the finite volume method. (This method is chosen because it allows the mass balance condition to be satisfied exactly.) The step-by-step algorithm based on the foregoing equations is coded and implemented into ABAQUS, to simulate the process of hydraulic fracturing with crack branching. In the present study, only a two-dimensional (2D) analysis of a square layer with a zero strain and a zero fluid flux in the transverse direction is conducted. The layer has a unit thickness and dimensions 5×5 m.

Attached to the boundary nodes of the shale layer are imaginary elastic springs of a stiffness equal to the stiffness of the surrounding infinite 2D domain of shale under the assumption of homogenous expansion within the layer. The resultants of the tectonic stresses $\sigma_h = 30$ MPa and $\sigma_H = 40$ MPa are applied to the boundary springs. The boundary condition of fluid flow is the imperviousness of the layer boundaries. As shown in Fig. 5, a horizontal wellbore is assumed to lie at the bottom of the square.

The wellbore is considered to be perforated by detonations of shape charges grouped in three perforation clusters, as marked in the Fig. 5. The fracking fluid, which is considered to contain enough proppants to prevent crack closure, is considered to be injected at these three clusters with a controlled pressure $p_0(t)$, which begins with a rapid rise to 70 MPa (rapid but static, no emitted waves) and then is kept constant. The overburden pressure is $\sigma_{zz} = 80$ MPa.

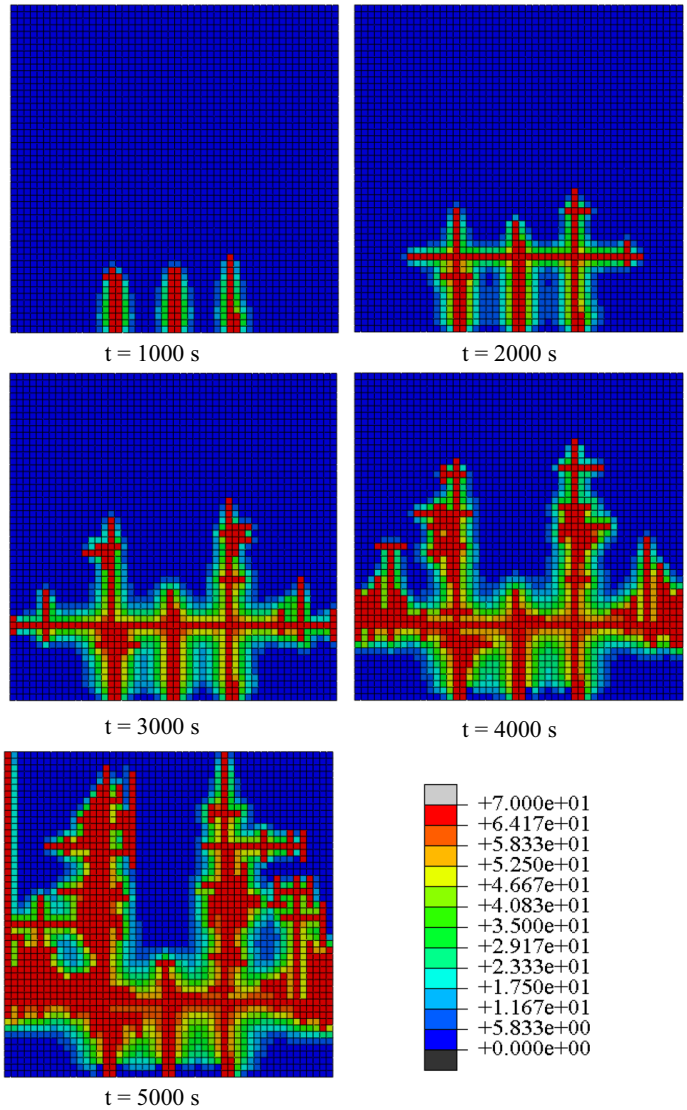

Fig. 10 The distribution of hydraulic pressure when the bedding layer orientation is 45° and with considering natural cracks

To study the influence of anisotropy of shale on the crack branching in the hydraulic fracturing process, three different kinds of 2D numerical models with bedding layer orientation 0°, 45° and 90° are studied, strictly for comparison purposes. (Admittedly, the second and third cases are artificial, not corresponding to practical situations, and should better be analyzed in three dimensions.)

Furthermore, to study the effect of closed preexisting natural cracks on the crack branching, for which the bedding layer inclination is of particular interest, two kinds of simulations are conducted for each case: one simulation without considering natural cracks and the other one with the natural cracks. These cracks are considered as vertical planes (or lines, in 2D) of zero strength and zero fracture energy, located at the planes of symmetry of each finite element.

The tensile strength of shale is dependent on the bedding layer orientation. When the bedding layer orientation is 0°, 45° and 90°, the tensile strengths are 3, 4 and 6 MPa, respectively. The strengths of these natural cracks are defined as 50 times smaller than the foregoing values, i.e., virtually as zero. Their damage factors w_1 and w_2 are raised gradually from 0 to 1 as soon as the tensile inelastic strain begins (Fig. 4). The simulation results are illustrated in Figs. 6, 7, 8, 9, 10 and 11.

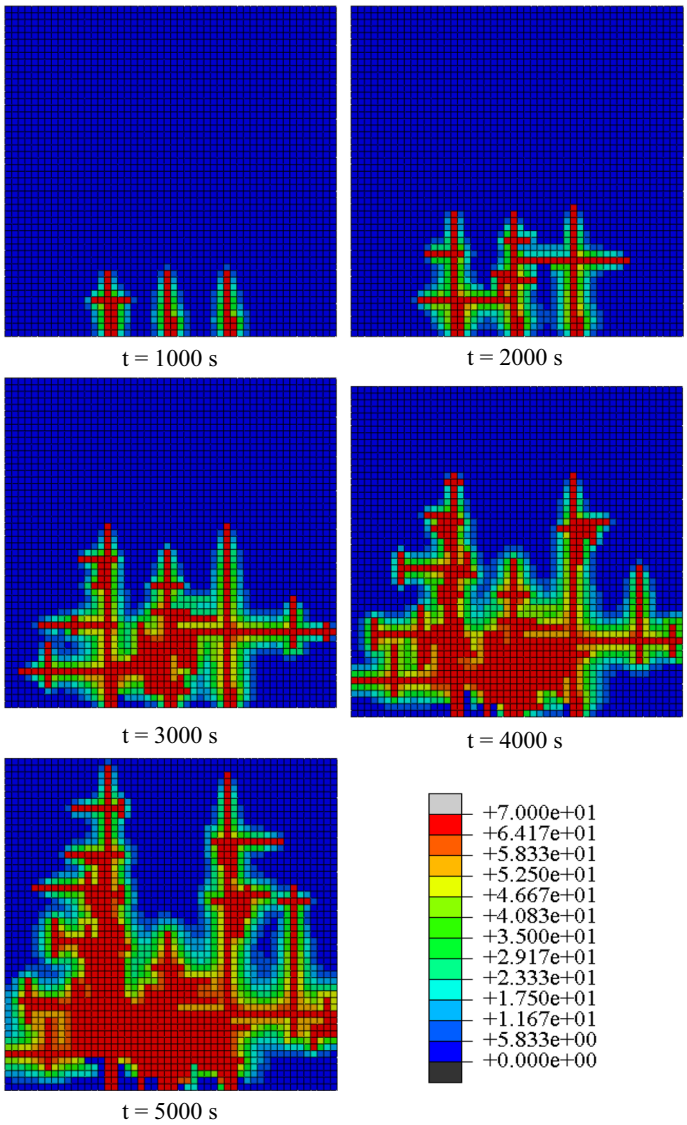

Fig. 11 The distribution of hydraulic pressure when the bedding layer orientation is 90° and with considering natural cracks

Figures 6, 7 and 8 show the evolving patterns of hydraulic pressure for bedding layer orientations 0°, 45° and 90° without considering the natural fractures, i.e., patterns in intact shale. The elements with the highest pressure (shown in red) reveal the open hydraulic cracks.

Initially, three cracks propagate synchronously in the minimum tectonic stress direction. Later only the cracks on both sides propagate, while the middle crack tends to stop. This is a manifestation of crack system instability [2] and has been empirically known as the stress-shadow effect [46,47]. No surprise, the cracks prefer to propagate along the minimum tectonic stress direction.

In all the cases, all the hydraulic fracturing generates crack branching except in the middle crack for the 90° bedding layer inclination (Fig. 8). The crack branching appears to be easier for bedding layer inclination 45° than for the other two orientations, in which the final crack network is less complicated. As expected, the bedding layer orientation is shown to have an effect on the crack branching.

Figures 9, 10 and 11 illustrate, for bedding layer inclinations 0°, 45° and 90°, the hydraulic crack networks when closed natural cracks of negligible strength exist in certain finite elements. Compared to the previous simulation for no natural cracks (Figs. 6, 7, 8), the cracks network is more complicated and the crack density is higher. Comparing with Fig. 8, the middle crack for bedding layer orientation 90° (Fig. 11) propagates farther along the minimum tectonic stress direction and generates more crack branching.

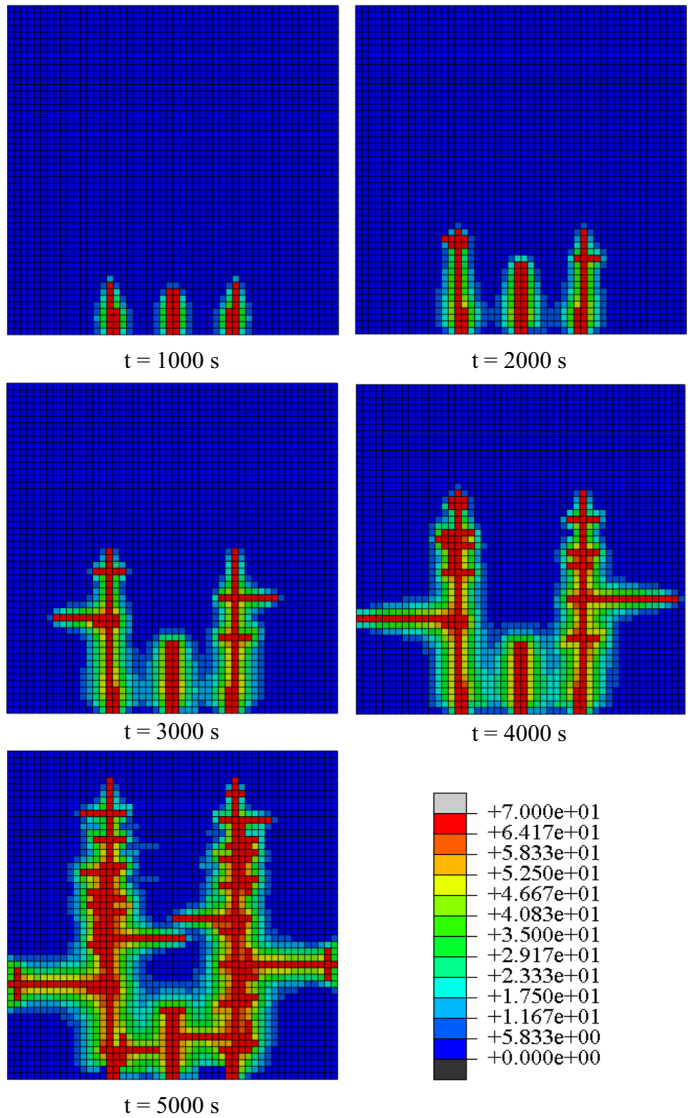

Fig. 12 The distribution of hydraulic pressure as assuming the reservoir is isotropic

As expected, it is easier to generate the crack branching when the natural cracks are considered. But the difference between the presence and absence of preexisting natural cracks of negligible strength is surprisingly small. Obviously, the main obstacle to hydraulic crack propagation at the depth of several kilometers is the tectonic stress, not the strength of shale.

It must be emphasized that the differences identified above are doubtless greatly limited by the 2D simplification. When the bedding layers have out-of-plane inclinations 45° or 90°, the preferred water flow and hydraulic crack would be out of plane. This, of course, cannot be captured with a 2D numerical model and must await the development of 3D program. Once the 3D simulations are conducted, one may expect a much stronger effect of anisotropy.

To assess the importance of anisotropy for the 2D hydraulic fracture propagation and branching, consider a hypothetical isotropic shale stratum obtained by changing the transverse elastic modulus so that $E_{zz} = E_{xx} = E_{yy}$, and setting the Poisson ratio as 0.13 (for Longmaxi shale). Also, the functions $f(\theta)$, $g(\theta)$ and $h(\theta)$ that make the stress–strain boundaries dependent on microplane dip angle θ (Fig. 2) are replaced by a value corresponding to the average effect of θ in the range from 0 to 90°.

The simulation results are illustrated in Fig. 12. Comparing this figure to Fig. 6, one can see that, in this 2D analysis, the crack branching in the isotropic case is less pronounced than it is in the anisotropic case. Also,

the final crack density is slightly higher in the anisotropic case. Although the difference between the isotropic and anisotropic cases is small, it is seen not to be negligible. A much stronger difference is expected for the 3D analysis (which is beyond the scope of this paper).

8 Summary and conclusions

1. Unlike most previous simulations of hydraulic fracturing, the model reviewed here can capture both the inelastic deformation and the inherent anisotropy of shale, the latter being reproduced by the spherocylindrical microplane model.
2. It is important that two kinds of water flow are considered: one is the Darcy diffusion flow in the pores or microcracks, and the other one is the Poiseuille flow through the hydraulic fractures and natural cracks. The Darcy flow can change the stress field significantly and is necessary to generate the crack branching.
3. The crack width is computed by means of the crack band model, in which each element is imagined to contain at the outset a potential cohesive crack, one in each direction, with fracking fluid flowing through if the crack gets opened. This model can avoid the problems of strain localization and spurious mesh sensitivity in simulation.
4. The present 2D simulations show a nonnegligible, though not very large, difference of fracture pattern evolutions between the formation with natural cracks and without natural cracks. But this difference is expected to be greater in 3D simulation.
5. Computer simulations limited to two dimensions show appreciable effects of anisotropy on the evolution of branched fracture pattern. However, a final appraisal of the anisotropy effects must wait for 3D simulations which are more demanding.

Acknowledgements Partial financial support from the US Department of Energy through Subcontract No. 37008 of Northwestern University with Los Alamos National Laboratory is gratefully acknowledged. The simulation of fracturing damage also received some support from ARO Grant W911NF-15-101240 to Northwestern University. The first author wishes to thank the Department of Science and Technology of Sichuan Province (Nos. 2015JY0280, 2012FZ0124) and CSC for supporting him as a Research Fellow at Northwestern University. Collaboration with Sichuan University which led to important understanding of Longmaxi shale is deeply appreciated.

References

1. Beckwith, R.: Hydraulic fracturing: the fuss, the facts, the future. J. Pet. Technol. **62**(12), 34–40 (2010)
2. Bažant, Z.P., Salviato, M., Chau, V.T., Viswanathan, H., Zubelewicz, A.: Why fracking works. J. Appl. Mech.-Trans. ASME. **81**(10), 101010-1–101010-10 (2014)
3. Xie, H.P., Gao, F., Ju, Y., Xie, L.Z., Yang, Y.M., Wang, J.: Novel idea of the theory and application of 3D volume fracturing for stimulation of shale gas reservoirs. Chin. Sci. Bull. **61**(1), 36–46 (2016)
4. Mokhtari, M., Bui, B.T., Tutuncu, A.N.: Tensile failure of shales: impacts of layering and natural fractures. In: SPE Western North American and Rocky Mountain Joint Meeting, Society of Petroleum Engineers (2014)
5. Niandou, H., Shao, J.F., Henry, J.P., Fourmaintraux, D.: Laboratory investigation of the mechanical behaviour of Tournemire shale. Int. J. Rock Mech. Min. Sci. **34**(1), 3–16 (1997)
6. Masri, M., Sibai, M., Shao, J.F., Mainguy, M.: Experimental investigation of the effect of temperature on the mechanical behavior of tournemire shale. Int. J. Rock Mech. Min. Sci. **70**, 185–191 (2014)
7. Heng, S., Guo, Y.T., Yang, C.H., Daemen, J.J.K., Li, Z.: Experimental and theoretical study of the anisotropic properties of shale. Int. J. Rock Mech. Min. Sci. **74**, 58–68 (2015)
8. Sone, H.: Mechanical properties of shale gas reservoir rocks, and its relation to the in-situ stress variation observed in shale gas reservoirs. Ph.D. thesis, Stanford University (2012)
9. Rassouli, F., Zoback, M.: A comparison of short-term and long-term creep experiments in unconventional reservoir formations. In: 50th US Rock Mechanics/Geomechanics Symposium, American Rock Mechanics Association (2016)
10. Tsai, S.W., Wu, E.M.: A general theory of strength for anisotropic materials. J. Compos. Mater. **5**(1), 58–80 (1971)
11. Hill, R.: The Mathematical Theory of Plasticity, vol. 11. Oxford University Press, Oxford (1998)
12. Lee, Y.K., Pietruszczak, S.: Tensile failure criterion for transversely isotropic rocks. Int. J. Rock Mech. Min. Sci. **79**, 205–215 (2015)
13. Rao, K.S., Rao, G.V., Ramamurthy, T.: A strength criterion for anisotropic rocks. Ind. Geotech. J. **16**(4), 317–333 (1986)
14. Jaeger, J.C.: Shear failure of anistropic rocks. Geol. Mag. **97**(1), 65–72 (1960)
15. Hoek, E.: Strength of jointed rock masses. Geotechnique **33**(3), 187–223 (1983)
16. Duveau, G., Shao, J.F., Henry, J.: Assessment of some failure criteria for strongly anisotropic geomaterials. Mech. Cohesive-Frict. Mater. **3**(1), 1–26 (1998)
17. Jin, W.C., Xu, H., Arson, C., Busetti, S.: Computational model coupling mode ii discrete fracture propagation with continuum damage zone evolution. Int. J. Numer. Anal. Methods Geomech. **41**(2), 223–250 (2016)

18. Levasseur, S., Welemane, H., Kondo, D.: A microcracks-induced damage model for initially anisotropic rocks accounting for microcracks closure. Int. J. Rock Mech. Min. Sci. **77**, 122–132 (2015)
19. Jin, W.C., Arson, C.: Discrete equivalent wing crack based damage model for brittle solids. Int. J. Solids Struct. **110**, 279–293 (2017)
20. Ravi-Chandar, K., Knauss, W.: An experimental investigation into dynamic fracture, III. On steady-state crack propagation and crack branching. Int. J. Fract. **26**(2), 141–154 (1984)
21. Garagash, D., Detournay, E.: The tip region of a fluid-driven fracture in an elastic medium. J. Appl. Mech.-Trans. ASME **67**(1), 183–192 (2000)
22. Bunger, A.P., Detournay, E., Garagash, D.I.: Toughness-dominated hydraulic fracture with leak-off. Int. J. Fract. **134**(2), 175–190 (2005)
23. Detournay, E.: Propagation regimes of fluid-driven fractures in impermeable rocks. Int. J. Geomech. **4**(1), 35–45 (2004)
24. Lecampion, B., Desroches, J.: Simultaneous initiation and growth of multiple radial hydraulic fractures from a horizontal wellbore. J. Mech. Phys. Solids. **82**, 235–258 (2015)
25. Wang, H.: Poro-elasto-plastic modeling of complex hydraulic fracture propagation, simultaneous multi-fracturing and producing well interference. Acta Mech. **227**(2), 507–525 (2016)
26. Waters, G.A., Lewis, R.E., Bentley, D.: The effect of mechanical properties anisotropy in the generation of hydraulic fractures in organic shales. In: SPE Annual Technical Conference and Exhibition. Society of Petroleum Engineers (2011)
27. Nagel, N.B., Sanchez-Nagel, M.A., Zhang, F., Garcia, X., Lee, B.: Coupled numerical evaluations of the geomechanical interactions between a hydraulic fracture stimulation and a natural fracture system in shale formations. Rock Mech. Rock Eng. **46**(3), 581–609 (2013)
28. Chau, V.T., Bažant, Z.P., Su, Y.W.: Growth model for large branched three-dimensional hydraulic crack system in gas or oil shale. Phil. Trans. R. Soc. A. **374**(2078), 20150418 (2016)
29. Chau, V.T., Li, C.B., Rahimi-Aghdam, S., Bažant, Z.P.: The enigma of large-scale permeability of gas shale: pre-existing or frac-induced? J. Appl. Mech.-Trans. ASME. **84**(6), 061008-1–061008-11 (2017)
30. Li, C.B., Caner, F.C., Chau, V.T., Bažant, Z.P.: Spherocylindrical microplane constitutive model for shale and other anisotropic rocks. J. Mech. Phys. Solids. **103**, 155–178 (2017)
31. Bažant, Z.P.: Comment on orthotropic models for concrete and geomaterials. J. Eng. Mech. **109**(3), 849–865 (1983)
32. Brocca, M., Bažant, Z.P., Daniel, I.M.: Microplane model for stiff foams and finite element analysis of sandwich failure by core indentation. Int. J. Solids Struct. **38**, 8111–8132 (2001)
33. Cusatis, G., Beghini, H., Bažant, Z.P.: Spectral stiffness microplane model for quasi-brittle composite laminates. I. Theory. J. Appl. Mech.-Trans. ASME **75**(1), 021009-1–021009-9 (2008)
34. Šmilauer, V., Hoover, C.G., Bažant, Z.P., Caner, F.C., Waas, K.W., Shahwan, K.: Multiscale simulation of fracture of braided composites via repetitive unit cell. Eng. Fract. Mech. **78**(6), 901–918 (2011)
35. Kirane, K., Salviato, M., Bažant, Z.P.: Microplane-triad model for elastic and fracturing behavior of woven composites. J. Appl. Mech.-Trans. ASME **83**(4), 041006-1–041006-14 (2016)
36. Bažant, Z.P., Oh, B.H.: Efficient numerical integration on the surface of a sphere. ZAMM-J. Appl. Math. Mech. **66**(1), 37–49 (1986)
37. Caner, F.C., Bažant, Z.P.: Microplane model M7 for plain concrete. I. Formulation. J. Eng. Mech. **139**(12), 1714–1723 (2013)
38. Bažant, Z.P., Xiang, Y.Y., Prat, P.C.: Microplane model for concrete. I: stress–strain boundaries and finite strain. J. Eng. Mech. **122**(3), 245–254 (1996)
39. Freeman, C., Moridis, G., Blasingame, T.: A numerical study of microscale flow behavior in tight gas and shale gas reservoir systems. Transp. Porous Media **90**(1), 253–268 (2011)
40. Ilgen, A.G., Heath, J.E., Akkutlu, I.Y., Bryndzia, L.T., Cole, D.R., Kharaka, Y.K., Kneafsey, T.J., Milliken, K.L., Pyrak-Nolte, L.J., Suarez-Rivera, R.: Shales at all scales: exploring coupled processes in mudrocks. Earth-Sci. Rev. **166**, 132–151 (2017)
41. Bažant, Z.P.: Crack band model for fracture of geomaterials. In: Eisenstein, Z. (eds.) Proceedings of 4th International Conference on Numerical Methods on Geomechanics, vol. 3. University of Alberta, Edmonton, pp 1137–1152 (1982)
42. Bažant, Z.P., Oh, B.H.: Crack band theory for fracture of concrete. Mater. Struct. **16**(3), 155–177 (1983)
43. Červenka, J., Bažant, Z.P., Wierer, M.: Equivalent localization element for crack band approach to mesh-sensitivity in microplane model. Int. J. Numer. Methods Eng. **62**(5), 700–726 (2005)
44. Bažant, Z.P., Planas, J.: Fracture and Size Effect in Concrete and Other Quasibrittle Materials. CRC Press, Boca Raton and London (1998)
45. Hull, K.L., Abousleiman, Y.N., Han, Y., Al-Muntasheri, G.A., Hosemann, P., Parker, S.S., Howard, C.B.: Nanomechanical characterization of the tensile modulus of rupture for kerogen-rich shale. SPE Journal. SPE-177628-PA (2017)
46. Sneddon, I.N.: The distribution of stress in the neighborhood of a crack in an elastic solid. Proc. R. Soc. A: Math. Phys. Eng. Sci. **187**(1009), 229–260 (1946)
47. Dohmen, T., Zhang, J., Blangy, J.P.: Measurement and analysis of 3D stress shadowing related to the spacing of hydraulic fracturing in unconventional reservoirs. SPE Annual Technical Conference and Exhibition, Society of Petroleum Engineers (2014)